Investigations on the Structural, Morphological, Electrical, and Magnetic Properties of $CuFe_2O_4$−NiO Nanocomposites

Ramakrishnan Kalai Selvan,*[,†,||] Venkata Krishnan,[‡,⊥] Chanassery Ouso Augustin,[†] Helmut Bertagnolli,[‡] Chul Sung Kim,[§] and Aharon Gedanken[||]

Electropyrometallurgy Division, Central Electrochemical Research Institute, Karaikudi 630 006, Tamil Nadu, India; Institute of Physical Chemistry, University of Stuttgart, Pfaffenwaldring 55, 70569 Stuttgart, Germany; Department of Physics, Kookmin University, Seoul 136-702, Korea; and Department of Chemistry and Kanbar Laboratory for Nanomaterials, Bar-Ilan University Center for Advanced Materials and Nanotechnology, Bar-Ilan University, Ramat-Gan 52900, Israel

Received July 19, 2007. Revised Manuscript Received November 21, 2007

$CuFe_2O_4$−xNiO (x = 1, 5, 10, and 20 wt %) nanocomposites have been successfully prepared by a simple combustion method using urea−nitrate precursors. The samples were sintered at different temperatures, namely 600, 800, 1000, and 1100 °C, for 5 h to enhance the compound formation and phase purity, studied by means of XRD patterns. Then the 1100 °C sintered sample was further characterized for its structural (EXAFS, XANES, FT-IR, UV–vis), morphological (SEM, TEM, HRTEM, SAED), electrical (ac conductivity, dielectric constant, dielectric loss tangent), and magnetic (Mössbauer) properties. The EXAFS and XANES studies reveal the formation of $NiFe_2O_4$ and CuO, in addition to the existence of $CuFe_2O_4$ and NiO phases. A partial substitution of metal cations by nickel ions could also be evidenced. The stretching and bending vibration of the tetrahedral and octahedral complexes have been established from FT-IR spectra. The UV–vis spectra elucidate that the prepared materials are semiconductors and also show the quantum size confinement effect. The well-defined grain and grain boundary structure was identified from the SEM studies. The nanosize of the synthesized materials has been identified by TEM investigations. The HRTEM and SAED images reveal the crystallinity and polycrystalline behavior of the as-synthesized materials. The electrical studies show the normal ferrimagnetic behavior of the materials. The inverse spinel nature of the materials has been enumerated from Mössbauer spectra, which also illustrates the phase transition behavior.

1. Introduction

Advanced novel materials are essential for various applications, where nanosize and tailor-made properties play a vital role. Hence, synthesis and characterization of nanostructured materials have become imperative for the advancement of science and technology. The manipulation of physical and chemical properties of the materials is one of the challenging areas in physics, chemistry, and materials science. The specific properties of the materials such as structural, electrical, optical, magnetic, and electrochemical properties mainly depend upon the size and shape of the nanoparticles. Therefore, the particle size and shape are considered as crucial parameters for the nanomaterials in novel applications.

Among the different categories of nanomaterials, transition metal oxide based ferrites (AFe_2O_4) have significant and insatiable interest in different fields.[1] It is well-known that spinel ferrites are highly resistive materials; hence, they are used as microwave and magnetic devices.[2] But nowadays, these materials can be used in multifarious applications by tuning their properties through modifying the particle size and shape, suitable substitution, and forming different composites. Some of the recent applications of nanosized ferrites and its composites are solar cell (Fe_3O_4),[3] drug delivery system (Fe_3O_4),[4] electrodes for supercapacitors (Fe_3O_4, $MnFe_2O_4$),[5,6] spintronic devices (Fe_3O_4, $CoFe_2O_4$, $NiFe_2O_4$),[7,8] anticorrosion pigments ($ZnFe_2O_4$, $MgFe_2O_4$),[9,10] isolation and purification of genomic DNAs ($CoFe_2O_4$),[11]

* Corresponding author. E-mail: selvankram@rediffmail.com.
† Central Electrochemical Research Institute.
‡ University of Stuttgart.
§ Kookmin University.
|| Bar-Ilan University.
⊥ Current address: Department of Chemistry, University of Pennsylvania, 231 South 34th Street, Philadelphia, PA 19104.

(1) Caruntu, G.; Bush, G. G.; O'Connor, C. J. *J. Mater. Chem* **2004**, *14*, 2753.
(2) Goldman, A. *Modern Ferrite Technology*; Van Nostrand Reinhold: New York, 1990.
(3) Rastogi, A. C.; Dhara, S.; Das, B. K. *J. Electrochem. Soc.* **1995**, *142*, 3148.
(4) Liu, T. Y.; Hu, S. H.; Liu, K. H.; Liu, D. M.; Chen, S. Y. *J. Magn. Magn. Mater.* **2007**, *310*, 2850.
(5) Chung, K. W.; Kim, K. B.; Han, S. H.; Lee, H. *Electrochem. Solid State Lett.* **2005**, *8*, A259.
(6) Kuo, S. L.; Wu, N. L. *Electrochem. Solid State Lett.* **2005**, *8*, A495.
(7) Stomer, M.; Singh, S. P.; Perez, O. P.; Guzman, R. P.; Calderson, E.; Remos, C. R. *Microelectron. J.* **2005**, *36*, 475.
(8) Lüders, U.; Barthélémy, A.; Bibes, M.; Bouzehouane, K.; Fusil, S.; Contour, J. P.; Bobo, J. F.; Fontcuberta, J.; Fert, A. *Adv. Mater.* **2006**, *13*, 1733.
(9) Yang, G. Q.; Han, B.; Sun, Z. T.; Yan, L. M.; Wang, X. Y. *Dyes Pigm.* **2002**, *55*, 9.
(10) Kalendova, A.; Vesely, D.; Brodinova, J. *Anti-Corros. Methods Mater.* **2004**, *51*, 6.
(11) Proodelalova, J.; Rittich, B.; Petrova, K.; Benes, M. J. *J. Chromotagr.* **2004**, *1056*, 43.

10.1021/cm701937q CCC: $40.75
Published on Web 12/28/2007

adsorbent for azo dye acid red B ($MnFe_2O_4$),[12] petroleum gas sensor ($NiFe_2O_4$),[13] negative electrodes for Li-ion batteries ($ZnFe_2O_4$, $NiFe_2O_4$, $CaFe_2O_4$, $CuFe_2O_4-SnO_2$),[14–17] gas sensors ($NiFe_2O_4$, $Mg_{1-x}Sn_xMo_yFe_{2-y}O_4$),[18,19] inert anodes for aluminum electrolysis ($NiFe_2O_4$, $Ni_{1-x}Mg_xFe_2O_4$),[20,21] catalyst for oxidation of organic compounds ($Cu_{1-x}Co_xFe_2O_4$),[22] humidity sensors ($Mg_{0.5}Cu_{0.5}Fe_2O_4$),[23] biosensors ($MnFe_2O_4$),[24] antimicrobial agent ($NiFe_2O_4-TiO_2$),[25] and many others.

Considering the various spinel ferrites, $CuFe_2O_4$ has gained a prominent interest among materials science researchers both fundamentally and technologically for various applications. Since Cu^{2+} is a Jahn–Teller ion, it gives the anomalous favorable properties and also exhibits phase transition from tetragonal to cubic, depending on the temperature. Many authors have reported the synthesis of nanosized $CuFe_2O_4$ using various synthetic methods based on wet chemical and dry processes. Recently, Qi et al.[26] have prepared 10 nm thick $CuFe_2O_4$ nanowalls by electrochemical method using bulk $CuFe_2O_4$ ceramic grains and found a phase transition behavior of tetragonal to cubic when the ceramic grains are converted into nanostructured $CuFe_2O_4$. Goya et al.[27] have proved that mechanical milling is a useful tool for preparing nanocrystalline $CuFe_2O_4$ from CuO and metallic ^{57}Fe with HNO_3. Their Mössbauer spectra reveals that the 48 h milled material gives the tetragonal structure with a particle size of 9.3 nm. Nanocrystalline $CuFe_2O_4$ with a particle size of 10–40 nm has been prepared by Gajbhiye et al.[28] using the coprecipitation method from chloride precursors and found that the cubic to tetragonal phase transition occurs at 973 K. The $CuFe_2O_4$ nanorod has been prepared by Huang et al.[29] using simple sol–gel technique with some chemical modifications. Using the electrochemical method, the nanocrystalline $CuFe_2O_4$ with a particle size of 10–30 nm have been prepared by Sartale et al.[30,31] from both aqueous and nonaqueous electrolytes. The tetragonal phase Cu−ferrite nanorods have been prepared by Huang et al.[32] using ethylene glycol and hexamethyltriamine assisted sol–gel synthesis, and they found low saturation magnetization of 10.2 emu g^{-1} compared with the bulk nanoparticles of 35.6 emu g^{-1} due to the organic coatings on the nanoparticles. Du et al.[33] have synthesized single crystal copper ferrite nanorods and nanodisks using the reverse micelle and hydrothermal method. The prepared nanorods are 40–60 nm in diameter and 180 nm in length, and the nanodisks were composed of quasi-hexagonal particles. Using X-ray absorption fine structure (XAFS) and X-ray diffraction (XRD) studies, Gomes et al.[34] have shown that the nanocrystalline $CuFe_2O_4$ has a mixed spinel structure with a cation distribution of $(Cu_{0.2}Fe_{0.8})_A[Cu_{0.8}Fe_{1.2}]_BO_4$ in the material prepared by the coprecipitation method.

Recently, synthesis and application of magnetic nanocomposites are a subject of intense research because of their unique properties, which makes them very appealing from both the scientific view of understanding their properties and the technological significance of enhancing the performance of new materials. Nanocomposite is an innovative material compared with the simple and substituted ferrites. It is a new class of material that has emerged in very recent years. Different types of ferrite-based composites have been studied which includes magnetic ferrites composed with nonmagnetic oxides and polymers. Some of the reported types of nanocomposites are magnetic−metal (Fe_3O_4-Au),[35] magnetic−oxide ($CoFe_2O_4-SiO_2$),[36] magnetic−polymer ($CoFe_2O_4$−polypyrolle),[37] magnetic−semiconductor (Fe_3O_4-PbS),[38] magnetic−alloy ($(Ni_{0.5}Zn_{0.5})Fe_2O_4-FeNi_3$),[39] magnetic−zeolite,[40] etc. The composite may be in the form of coating, pinning, oriented attachment, and core–shell structure of ferrites with the nanoparticles. Properties of these nanocomposites not only depend upon the elemental and phase composition of the materials but also on the size, shape, and crystallographic orientations of grains. Among the transition metals NiO has many potential applications such as catalyst, battery cathodes, gas sensor materials, electrochromic films,

(12) Wu, R.; Qu, J. *J. Chem. Technol. Biotechnol.* **2005**, *80*, 20.
(13) Satyanarayana, L.; Manorama, S. V. *Mater. Chem. Phys.* **2003**, *82*, 21.
(14) NuLi, Y. N.; Qin, Q. Z. *J. Power Sources* **2005**, *142*, 292.
(15) Yang, X.; Wang, X.; Zhang, Z. *J. Cryst. Growth* **2005**, *277*, 467.
(16) Alcántara, R.; Jaraba, M.; Lavela, P.; Tirado, J. L.; Jumas, J. C.; Fourcade, J. O. *Electrochem. Commun.* **2003**, *5*, 16.
(17) Selvan, R. K.; Kalaiselvi, N.; Augustin, C. O.; Doh, C. H. *Electrochem. Solid State Lett.* **2006**, *9*, A390.
(18) Liu, Z.; Liu, Y.; Yang, Y.; Shen, G.; Yu, R. *Anal. Chim. Acta* **2005**, *533*, 3.
(19) Rezlescu, N.; Doroftei, C.; Rezlescu, E.; Popa, P. D. *Phys. Status Solidi A* **2006**, *203*, 306.
(20) Li, Y.; Tao, Z.; Kechao, Z.; Yong, L.; Fang, L.; Fang, Z. *Anti-Corros. Methods Mater.* **2004**, *51*, 25.
(21) Berchmans, L. J.; Selvan, R. K.; Augustin, C. O. *Mater. Lett.* **2004**, *58*, 1928.
(22) Mathuo, T.; Shylesh, S.; Reddy, S. N.; Sebastin, C. P.; Date, S. K.; Rao, B. S.; Kulkarni, S. D. *Catal. Lett.* **2004**, *93*, 155.
(23) Rezlescu, N.; Rezlescu, E.; Sava, C. L.; Popa, P. D. *Phys. Status Solidi A* **2004**, *201*, 17.
(24) Grancharov, S. G.; Zeng, H.; Sun, S.; Wang, S. X.; O'Brien, S.; Murray, C. B.; Kirtley, J. R.; Held, G. A. *J. Phys. Chem. B* **2005**, *109*, 13030.
(25) Rana, S.; Misra, R. D. K. *J. Met.* **2005**, *12*, 65.
(26) Qi, J. Q.; Chen, W. P.; Lu, M.; Wang, Y.; Tian, H. Y.; Li, L. T.; Chen, H. L. W. *Nanotechnology* **2005**, *16*, 3097.
(27) Goya, G. F. *J. Mater. Sci. Lett.* **1997**, *16*, 563.
(28) Gajbhiye, N. S.; Balaji, G.; Bhattacharyya, S.; Ghafari, M. *Hyperfine Interact.* **2004**, *57*, 156–157.
(29) Huang, Z.; Zhu, Y.; Zhang, J.; Yin, G. *J. Phys. Chem. C* **2007**, *111*, 6821.
(30) Sartale, S. D.; Bagde, G. D.; Lokhande, C. D.; Giersig, M. *Appl. Surf. Sci.* **2001**, *82*, 366.
(31) Sartale, S. D.; Lokhande, C. D. *Mater. Chem. Phys.* **2001**, *70*, 274.
(32) Huang, Z.; Zhu, Y.; Wang, S.; Yin, Y. *Cryst. Growth Des.* **2006**, *6*, 1931.
(33) Du, J.; Liu, Z.; Wu, W.; Li., Z.; Han, B.; Huang, Y. *Mater. Res. Bull.* **2005**, *40*, 928.
(34) Gomes, J. A.; Sousa, M. H.; Silva, G. A.; Tourinho, F. A.; Filho, J. M.; Azevedo, M.; Depeyrot, J. *J. Magn. Magn. Mater.* **2006**, *300*, e213.
(35) Wang, J.; Luo, J.; Fan, Q.; Suzuki, M.; Suzuki, I. S.; Engelhard, M. H.; Lin, Y.; Kim, N.; Wang, J. Q.; Zhong, C. J. *J. Phys. Chem. B* **2005**, *109*, 21593.
(36) Casu, A.; Casula, M. F.; Corrias, A.; Falqui, A.; Loche, D.; Marras, S. *J. Phys. Chem. C* **2007**, *111*, 916.
(37) Murillo, N.; Ochoteco, E.; Alesanco, Y.; Pomposo, J. A.; Rodriguez, J.; Gonzalez, J.; Val, J. J. D.; Gonzaalez, J. M.; Brtel, M. R.; Lopez, A. R. A. *Nanotechnology* **2004**, *15*, S322.
(38) Shi, W.; Zeng, H.; Sahoo, Y.; Ohulchansky, T. Y.; Ding, Y.; Wang, Z. L.; Swihart, M.; Prasad, P. N. *Nano Lett.* **2006**, *6*, 875.
(39) Lu, X.; Liang, G.; Zhang, Y.; Zhang, W. *Nanotechnology* **2007**, *18*, 015701.
(40) Arruebo, M.; Pacheco, R. F.; Irusta, S.; Arbiol, J.; Ibarra, M.; Santamaraia, J. *Nanotechnology* **2006**, *151*, 4057.

fuel cell electrodes, etc.[41–46] NiO is a p-type semiconductor having wide band gap energy from 3.5 to 4.0 eV,[47] although stoichiometric NiO is an insulator with resistivity of the order of 10^{13} Ω cm at room temperature. The physical and chemical properties of the materials are mainly dependent on the size and its distribution.

A thorough literature survey has indicated that no detailed study has been carried out on $CuFe_2O_4$−NiO nanocomposites. Hence, considering the importance of these nanocomposites, this first comprehensive study highlights the synthesis and characterization of $CuFe_2O_4$−NiO nanocomposites in different compositions and sintered at different temperatures. The structural properties of the synthesized materials have been studied using X-ray diffraction, extended X-ray absorption fine structure (EXAFS), X-ray absorption near edge structure (XANES), Fourier transform infrared (FT-IR), and ultraviolet–visible (UV–vis) spectroscopic methods. Scanning electron microscopy (SEM) has been used to study the morphological properties. The nanometer size of the synthesized materials and nanocrystallinity have been investigated by means of transmission electron microscopy (TEM), high-resolution transmission electron microscopy (HRTEM), and selected area electron diffraction (SAED). In addition, the electrical properties such as ac conductivity, dielectric constant, and dielectric loss tangent have also been studied. Mössbauer spectroscopy has been employed to investigate the magnetic properties.

2. Experimental Section

2.1. Synthesis. Nanocomposites of $CuFe_2O_4$−xNiO (x = 0, 1, 5, 10, 20 wt %) were synthesized by the combustion method. The stoichiometric quantities of starting materials, viz., $Cu(NO_3)_2 \cdot 6H_2O$, $Fe(NO_3)_3 \cdot 9H_2O$, $Ni(NO_3)_2 \cdot 6H_2O$, and $CO(NH_2)_2$, were dissolved in 100 mL of distilled water. The mixed nitrate−urea solution was heated at 110 °C, with continuous stirring. After the evaporation of excess of water, a highly viscous gel (precursor) was obtained. Subsequently, the gel was ignited at 300 °C to evolve the undesirable gaseous products, and the process resulted in the formation of desired product in the form of foamy powder. Ultimately, the powder was sintered at different temperatures (600, 800, 1000, and 1100 °C) for 5 h to obtain ultrafine powders of $CuFe_2O_4$−NiO nanocomposites.

2.2. Characterization. The compound formation and crystallinity of the materials were identified by XRD patterns, which were obtained from a X-ray diffractometer (PANalytical, X'per PRO Cu Kα radiation; α = 1.5405 Å). The transmission mode XAFS measurements were performed on the nanocomposite ferrite samples at Cu K-edge at 8979 eV, Fe K-edge at 7112 eV, and Ni K-edge at 8333 eV at the beamline A1, at Hamburger Synchrotron Radiation Laboratory (HASYLAB), Hamburg, Germany. The samples were measured with a Si(111) double-crystal monochromator at ambient conditions, and ion chambers filled with nitrogen were used to measure the incident and transmitted intensities. The positron energy was 4.45 GeV, and the beam current was between 90 and 130 mA during the measurements. The samples in solid state were embedded in cellulose matrix and pressed into pellet, where the sample concentration was adjusted to yield an extinction of 1.5. The prepared pellets were encapsulated by Kapton tape and mounted onto sample holders for XAFS measurements. The details of data evaluation for extended X-ray absorption fine structure (EXAFS) and X-ray absorption near-edge structure (XANES) are presented in an earlier article.[48] In the EXAFS fitting procedure, the various parameters, i.e., coordination number, interatomic distance, Debye–Waller factor, and Fermi energy value, were determined by iterations. For clarity reasons, the EXAFS spectrum and the Fourier transform plot are shifted along the ordinate axis in many figures. The exact zero position of the EXAFS spectrum and that of the corresponding Fourier transform can be obtained by observing the value on the ordinate axis at the intersection point.

The FT-IR spectra of the samples were recorded with the KBr disks in the range of 400–1000 cm^{-1} using a Perkin-Elmer spectrophotometer (Perkin-Elmer, UK, Paragon-500 model). UV–vis spectroscopic measurements were carried out on a Cary Varian 1E spectrometer in the range of 200–800 nm. The nanometric particle size was analyzed through TEM (JEOL-JEM 100SX microscope at an accelerating voltage of 200 kV). The morphological features have been analyzed through SEM (JEOL S-3000 model). The measurement of electrical properties of the samples were performed at room temperature using impedance analyzer HIOKI 3532 controlled by a computer in the frequency range of 42 Hz−5 MHz. The powders were compacted with the addition of poly(vinylidene difluoride) (PVDF) binder in 1 cm diameter and 0.3 cm thickness pellets by using a hydraulic press applying a pressure of 3.5 tons cm^{-2}. Then the pellets were sintered at 150 °C for 2 h. The silver paint was coated on both sides of the pellet to act as a blocking electrode and also to provide the mechanical strength. The Mössbauer spectra were recorded using a conventional Mössbauer spectrometer of the electromechanical type with a 30 mCi ^{57}Co source in a Rh matrix.[49]

3. Results and Discussion

3.1. XRD Investigations. The XRD patterns of $CuFe_2O_4$−xNiO (x = 1, 5, 10, and 20 wt %) nanocomposites sintered at four different temperatures, namely 600, 800, 1000, and 1100 °C, are shown in Figure 1. The mean crystallite size was calculated from the width of the most intense diffraction peak using the Scherrer equation.[50] The obtained lattice parameter values along with the crystallite size are given in Table 1.

The XRD pattern of as-prepared (green) $CuFe_2O_4$−1% NiO (Figure 1a) sample shows the incomplete compound formation with broad peaks indicating the nanocrystalline nature of the materials. The samples sintered at 600 and 800 °C show some peaks due to impurities such as CuO and Fe_2O_3, which could be derived from the decomposition of nitrate precursors. To improve the crystallinity of the material, the samples were further sintered at 1000 and 1100 °C, which lead to the appearance of sharp and well-defined

(41) Ovshinsky, S. R.; Fetcenko, M. A.; Ross, J. *Science* **1993**, *260*, 176.
(42) Sheela, B.; Gomathi, H.; Rao, G. P. *J. Electroanal. Chem.* **1995**, *394*, 267.
(43) Yoshio, M.; Todorov, Y.; Yamato, K.; Noguchi, H.; Itoh, J.; Okada, M.; Mouri, T. *J. Power Sources* **1998**, *74*, 46.
(44) Dirksen, J. A.; Duval, K.; Ring, T. A. *Sens. Actuators B* **2001**, *80*, 106.
(45) Miller, E. L.; Rocheleau, R. E. *J. Electrochem. Soc.* **1997**, *144*, 3072.
(46) Makkus, R. C.; Hemmes, K.; Wir, J. H. W. D. *J. Electrochem. Soc.* **1994**, *141*, 3429.
(47) Boschloo, G.; Hagfeldt, A. *J. Phys. Chem. B* **2001**, *105*, 3039.
(48) Krishnan, V.; Selvan, R. K.; Augustin, C. O.; Gedanken, A.; Bertagnolli, H. *J. Phys. Chem. C* **2007**, *111*, 16724.
(49) An, S. Y.; Shim, I. B.; Kim, C. S. *J. Appl. Phys.* **2002**, *91*, 8465.
(50) (a) Scherrer, P. *Nachr. Ges. Wiss. Goettingen* **1918**, 96. (b) Klug, H. P.; Alexander, L. E. *X-Ray Diffraction Procedures for Polycristalline and Amorphous Materials*; J. Wiley & Sons: New York, 1974.

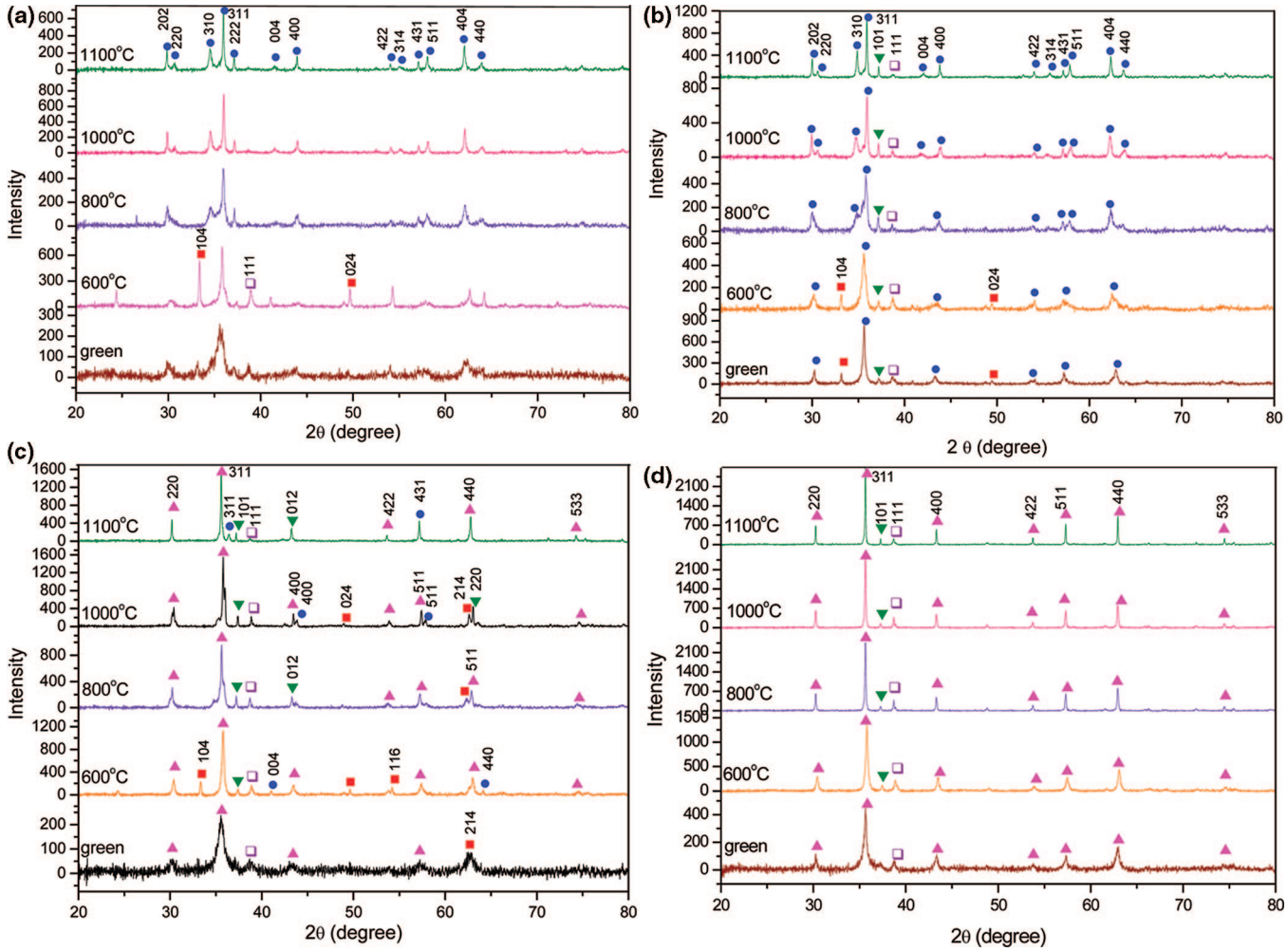

Figure 1. XRD patterns of $CuFe_2O_4$−xNiO nanocomposites, where (a) $x = 1$, (b) $x = 5$, (c) $x = 10$, and (d) $x = 20$ wt %: (●) $CuFe_2O_4$, (□) CuO, (▲) $NiFe_2O_4$,(■) Fe_2O_3, and (▼) NiO.

Table 1. Lattice Parameters Obtained from XRD for $CuFe_2O_4$−NiO Nanocomposites[a]

		sintering temperature [°C]				
sample		as-prepared	600	800	1000	1100
$CuFe_2O_4$−1% NiO	a [Å]	8.3221	8.2997	8.2684	8.2638	8.2743
	c [Å]	8.5207	8.3710	8.6046	8.6376	8.6516
	D [nm]	12	16	21	26	35
$CuFe_2O_4$−5% NiO	a [Å]	8.3499	8.3618	8.3089	8.2734	8.2863
	c [Å]	8.3490	8.3700	8.5385	8.6028	8.5496
	D [nm]	10	13	19	26	31
$CuFe_2O_4$−10% NiO	a [Å]	8.3348	8.3212	8.3555	8.2656	8.3631
	c [Å]	8.3798	8.3043	8.3467	8.4612	8.3627
	D [nm]	18	25	27	32	45
$CuFe_2O_4$−20% NiO	a [Å]	8.3441	8.3142	8.3482	8.3446	8.3478
	c [Å]	8.3512	8.3041	8.3440	8.3451	8.3478
	D [nm]	16	21	28	35	42

[a] a, c = lattice constants and D = crystallite size.

peaks corresponding to the planes of (202), (220), (310), (311), (222), (004), (400), (422), (314), (431), (511), (404), and (440), confirming the formation of single phase $CuFe_2O_4$.[48] Generally, the Bragg planes of (220) and (222) correspond to tetrahedral and (440) plane corresponds to octahedral sites.[51] It can be seen that the relative intensity of the I_{220} plane increases from 5.44 to 8.79 and I_{440} plane increases from 6.82 to 11.53 when compared with the parent $CuFe_2O_4$.[48] This is due to the reason that the added Ni^{2+} ions are substituted in B-sites by replacing the Fe^{3+} ions. Therefore, the excess Fe^{3+} ions in the B-site migrate to A-site due to the cation redistribution. Hence, the active cation concentrations of Fe^{3+} and Ni^{2+} ions are increased at both the sites, which in turn increases the intensity of corresponding planes. It can be concluded that the added Ni^{2+} ions are substituted on the B-site of parent $CuFe_2O_4$. The lattice constant values (refer Table 1) indicate the tetragonal structure, and the values are slightly changed with the addition of NiO due to the difference in the ionic radii.

(51) Augustin, C. O.; Hema, K.; Berchmans, L. J.; Selvan, R. K.; Saraswathi, R. *Phys. Status Solidi A* **2005**, *202*, 1017.

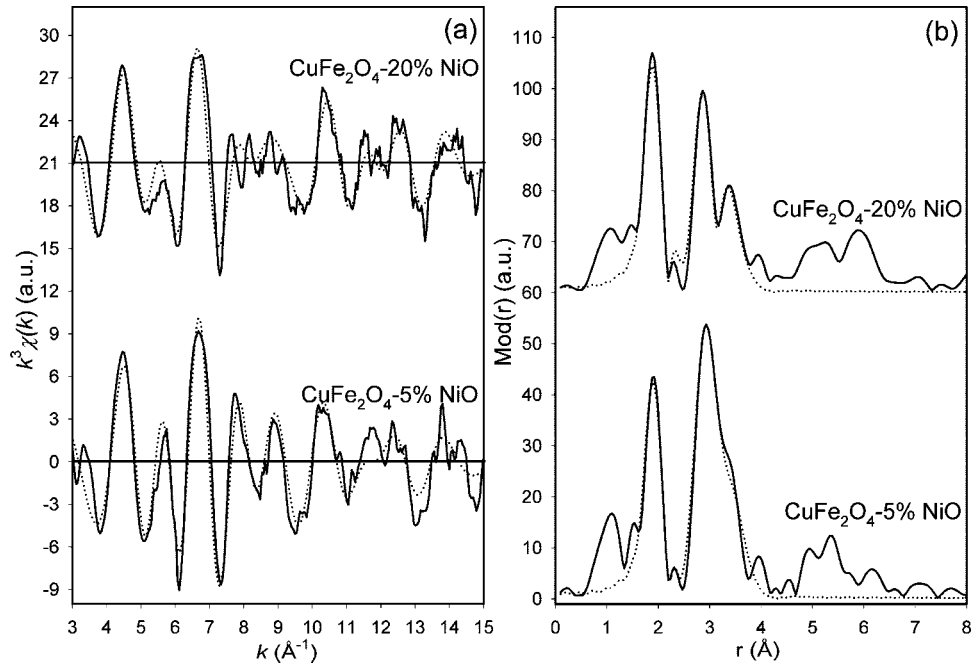

Figure 2. Experimental (—) and calculated (•••) EXAFS functions (a) and their Fourier transforms (b) for $CuFe_2O_4$−NiO nanocomposites measured at the Cu K-edge.

Table 2. EXAFS Obtained Structural Parameters for $CuFe_2O_4$−NiO Nanocomposites

sample	A−Bs[a]	N[b]	r[c] [Å]	σ[d] [Å]	E_F[e] [eV]	k-range [Å^{-1}]	R-factor
$CuFe_2O_4$−5% NiO	Cu−O	3.6 ± 0.4	1.98 ± 0.02	0.067 ± 0.007	6.888	2.96–15.03	41.03
	Cu−O	1.6 ± 0.2	2.20 ± 0.02	0.071 ± 0.007			
	Cu−M_B[f]	6.2 ± 1.0	2.93 ± 0.03	0.102 ± 0.015			
	Cu−M_A[g]	3.5 ± 0.7	3.43 ± 0.04	0.112 ± 0.022			
	Fe−O	5.0 ± 0.5	1.95 ± 0.02	0.110 ± 0.011	4.374	2.98–12.02	27.85
	Fe-M_B[f]	5.2 ± 0.8	2.98 ± 0.03	0.122 ± 0.018			
	Fe−$M_{A/B}$[h]	6.1 ± 1.2	3.47 ± 0.04	0.116 ± 0.023			
	Ni−O	6.6 ± 0.7	2.04 ± 0.02	0.067 ± 0.007	12.36	2.97–12.04	38.25
	Ni−M_B[f]	6.4 ± 1.0	2.92 ± 0.03	0.087 ± 0.013			
	Ni−M_A[g]	6.4 ± 1.3	3.43 ± 0.04	0.095 ± 0.019			
$CuFe_2O_4$−20% NiO	Cu−O	3.9 ± 0.4	1.97 ± 0.02	0.071 ± 0.007	4.944	2.97–15.02	42.79
	Cu−O	1.1 ± 0.1	2.18 ± 0.02	0.050 ± 0.005			
	Cu−M_B[f]	4.7 ± 0.7	2.93 ± 0.03	0.092 ± 0.014			
	Cu−Cu	3.4 ± 0.5	3.12 ± 0.03	0.095 ± 0.014			
	Cu−M_A[g]	2.0 ± 0.4	3.41 ± 0.04	0.105 ± 0.021			
	Fe−O	5.1 ± 0.5	1.95 ± 0.02	0.102 ± 0.010	4.412	2.98–12.02	32.33
	Fe−M_B[f]	6.0 ± 0.9	2.98 ± 0.03	0.118 ± 0.018			
	Fe−$M_{A/B}$[h]	6.0 ± 1.2	3.47 ± 0.04	0.092 ± 0.018			
	Ni−O	6.7 ± 0.7	2.03 ± 0.02	0.074 ± 0.007	12.22	2.98–12.04	44.85
	Ni−M_B[f]	6.4 ± 1.0	2.92 ± 0.03	0.087 ± 0.013			
	Ni−M_A[g]	6.4 ± 1.3	3.42 ± 0.04	0.095 ± 0.019			

[a] Absorber (A), backscatterers (Bs). [b] Coordination number N. [c] Interatomic distance r. [d] Debye–Waller factor σ with its calculated deviation. [e] Fermi energy E_F. [f] Metal backscatterers occupying the octahedral sites M_B. [g] Metal backscatterers occupying the tetrahedral sites M_A. [h] Metal backscatterers occupying both tetrahedral and octahedral sites $M_{A/B}$.

When the concentration of NiO increases from 1% to 5% (Figure 1b), the as-prepared sample gives large number of peaks corresponding to $CuFe_2O_4$, Fe_2O_3, NiO, and CuO. Actually, metal-induced crystallization (MIC) is an important phenomenon in the field of semiconductors for decreasing the compound formation temperature.[52] It can be seen that the metal oxide (NiO) can also induce the crystallization of $CuFe_2O_4$ at lower temperature, and it plays a vital role to act as a flux and to enhance the compound formation. As the sintering temperature increases from room temperature to 600 and to 800 °C, the compound formation also increases, which is evidenced by the increase in the intensity of the diffraction peaks. The lattice parameter values are changed with increasing sintering temperature, confirming the tetragonal structure. From the intensity calculation of 1100 °C sintered sample, I_{220} plane increases from 8.79 to 10.23 and I_{440} plane from 11.53 to 11.66. This result indicates the cation redistribution of Fe^{3+} ion on both the octahedral and tetrahedral sites.

At higher concentrations of 10% and 20% (Figure 1c,d), $CuFe_2O_4$−NiO nanocomposites show a very interesting behavior; i.e., the tetragonal structure is converted into cubic structure. This crystallographic transformation is attributed to the decrease in concentration of Jahn–Teller ion (Cu^{2+}) at the octahedral sites in the host structure, as a result of Ni^{2+} substitution which leads to the formation

(52) Perkas, N.; Pol, V. G.; Pol, S. V.; Gedanken, A. *Cryst. Growth Des.* **2006**, *6*, 293.

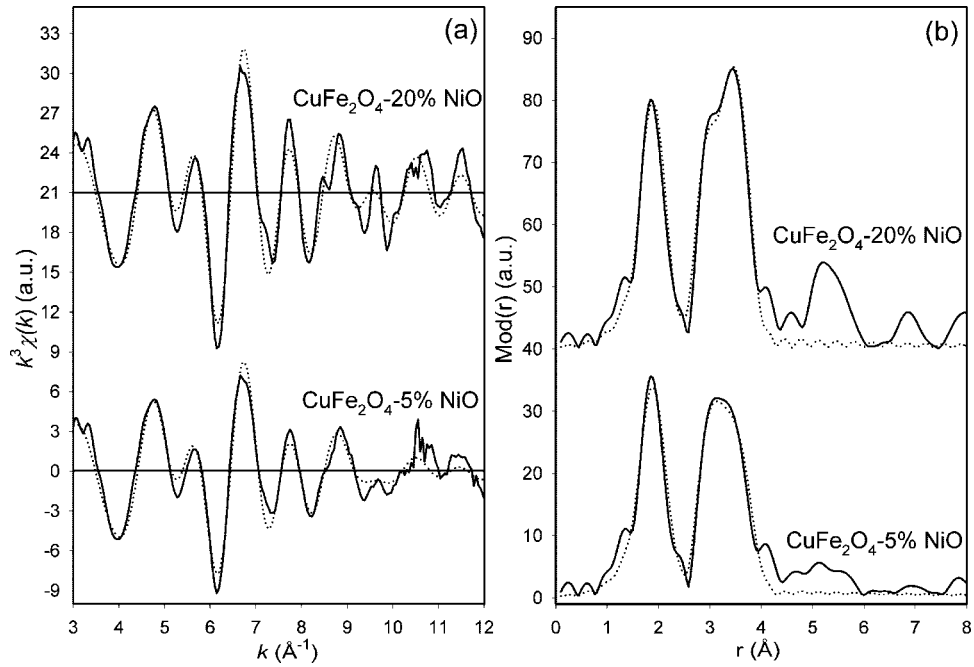

Figure 3. Experimental (—) and calculated (•••) EXAFS functions (a) and their Fourier transforms (b) for $CuFe_2O_4$−NiO nanocomposites measured at the Fe K-edge.

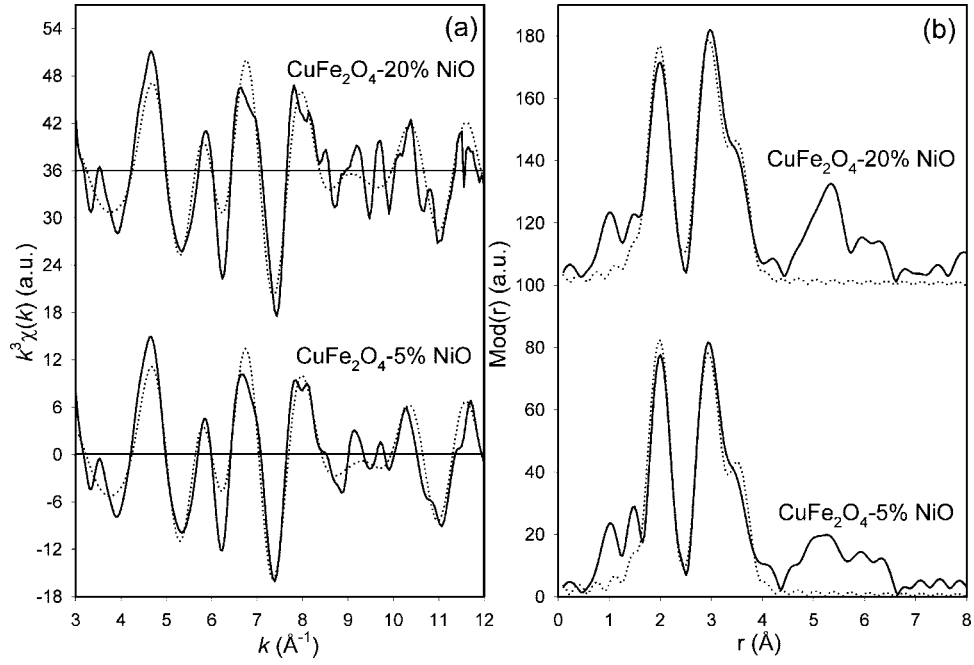

Figure 4. Experimental (—) and calculated (•••) EXAFS functions (a) and their Fourier transforms (b) for $CuFe_2O_4$−NiO nanocomposites measured at the Ni K-edge.

of high-symmetry phase of cubic structure. Similar types of observations was previously reported for Zn^{2+}-substituted $CuFe_2O_4$.[53] Two important phenomena are considered for the compound formation, i.e., effect of sintering and effect of additives. In general, the former is more predominant than the latter at higher temperature while at lower sintering temperature the additive effect is predominant. Similarly, at higher sintering temperature of 1100 °C the XRD pattern of $CuFe_2O_4$−10% NiO shows the maximum number of peaks for $NiFe_2O_4$ phase. As nickel and copper are near-neighbors in the periodic table, the peaks corresponding to $NiFe_2O_4$ and $CuFe_2O_4$ are very close to each other and have nearly the same 2θ values. So it was not possible to unambiguously distinguish these two phases from each other by XRD analysis. In this regard, more information was obtained from EXAFS analysis, which revealed the existence of the $CuFe_2O_4$, $NiFe_2O_4$, and other phases indicating the composite nature of these materials. Likewise, $CuFe_2O_4$−20% NiO sample also gives large number of peaks for $NiFe_2O_4$ along with

(53) Ata-Allah, S. S.; Hashhash, A. *J. Magn. Magn. Mater.* **2006**, *307*, 191.

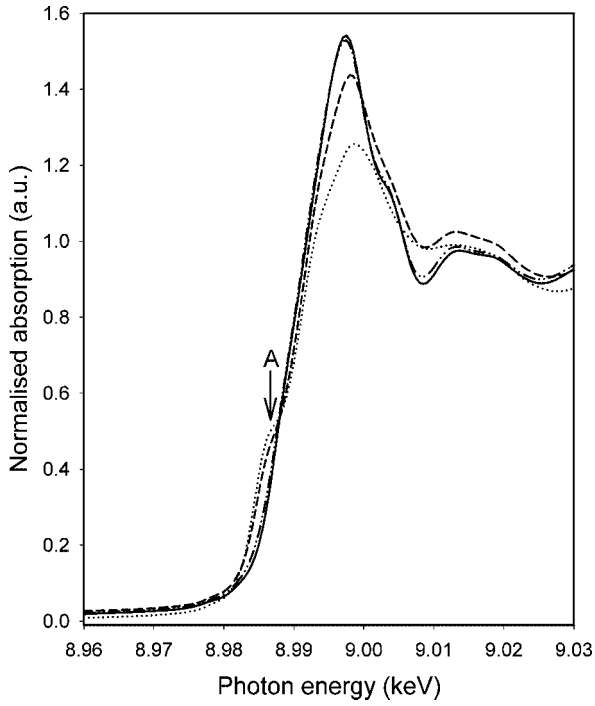

Figure 5. XANES region of $CuFe_2O_4$−5% NiO (-˙-) and $CuFe_2O_4$−20% NiO (---) along with the references $CuFe_2O_4$ (—) and CuO (•••) measured at the Cu K-edge.

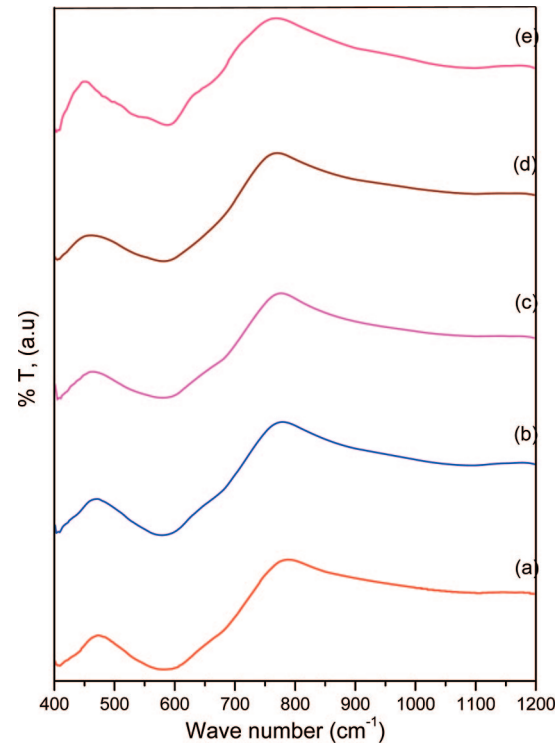

Figure 6. FT-IR spectra of $CuFe_2O_4$−x% NiO nanocomposites: (a) $x = 0$, (b) $x = 1$, (c) $x = 5$, (d) $x = 10$, and (e) $x = 20$.

NiO and CuO phases for all the sintering temperatures, revealing the effect of sintering as well as the additive effect. This exchange reaction could be attributed to the more negative Gibbs free energy formation of $NiFe_2O_4$ by NiO (−211.7 kJ/mol) and Fe_2O_3 (−740.568 kJ/mol) compared to the formation of $CuFe_2O_4$ by CuO (−129.7 kJ/mol) and Fe_2O_3 (−740.568 kJ/mol). Hence, the NiO + Fe_2O_3 → $NiFe_2O_4$ reaction is more favorable compared to the CuO + Fe_2O_3 → $CuFe_2O_4$ reaction.[54]

3.2. EXAFS Investigations. In order to obtain a deeper insight into the local structure of the $CuFe_2O_4$−NiO nanocomposites, EXAFS studies were performed on 5% and 20% samples sintered at 1100 °C. The experimentally determined and theoretically calculated EXAFS functions in *k*-space and their Fourier transforms in real space for 5 and 20 wt % NiO containing $CuFe_2O_4$ nanocomposites, measured at the Cu K-edge, are shown in Figure 2, and the determined structural parameters are tabulated in Table 2.

The EXAFS spectra obtained for 5% and 20% $CuFe_2O_4$−NiO nanocomposites are different from each other. The structural parameters obtained for 5% NiO containing $CuFe_2O_4$ nanocomposites are in agreement with those of $CuFe_2O_4$ nanoparticles.[48] But in the case of 20% NiO containing $CuFe_2O_4$ nanocomposites, a significant decrease in the coordination number of the metal backscatterers occupying the octahedral site (at 2.93 Å) and tetrahedral site (at 3.41 Å) could be observed, suggesting the partial substitution of the metal ions in these sites by nickel ions. Even though nickel ions preferentially occupy the octahedral sites, recent studies by Chkoundali et al.[55] on $NiFe_2O_4$ nanoparticles reveal that about 10% of nickel ions occupy the tetrahedral sites. It is known that, at the nanometer level, the coordination numbers strongly depend on the crystallite size. However, in the present case, the changes observed in the coordination numbers could not be attributed to the changes in the crystallite size, as the crystallites are very large and the size variation between the different nanocomposites is within the same order of magnitude. Furthermore, a new shell with copper backscatterers originates at 3.12 Å distance. This shell was not observed in the other $CuFe_2O_4$-based nanocomposites[48] and is in agreement with Cu−Cu distance of 3.10 Å in CuO.[56] This result suggests the formation of CuO during the preparation of $CuFe_2O_4$−20% NiO nanocomposites.

Table 3. Edge Energy and Oxidation States for $CuFe_2O_4$−NiO Nanocomposites along with the Reference Compounds

sample	element	oxidation state	absorption edge [eV]
$CuFe_2O_4$	Cu	+2	8991.0
	Fe	+3	7124.0
$CuFe_2O_4$−5% NiO	Cu	+2	8991.0
	Fe	+3	7123.5
	Ni	+2	8344.0
$CuFe_2O_4$−20% NiO	Cu	+2	8992.0
	Fe	+3	7124.0
	Ni	+2	8344.0
CuO	Cu	+2	8991.5
Fe_2O_3	Fe	+3	7124.0
FeO	Fe	+2	7119.5
NiO	Ni	+2	8343.5

(54) Yang, H.; Zhang, X.; Huang, C.; Yang, W.; Qiu, G. *J. Phys. Chem. Solids* **2004**, *65*, 1329.
(55) Chkoundali, S.; Ammar, S.; Jouini, N.; Fievet, F.; Molinie, P.; Danot, M.; Villain, F.; Greneche, J. M. *J. Phys.: Condens. Matter* **2004**, *16*, 4357.
(56) Asbrink, S.; Norrby, L. J. *Acta Crystallogr.* **1970**, *26*, 8.
(57) Harris, V. G.; Koon, N. C.; Williams, C. M.; Zhang, Q.; Abe, M.; Kirkland, J. P.; McKeown, D. A. *IEEE Trans. Magn.* **1995**, *31*, 3473.

Table 4. FT-IR and UV–vis Parameters for $CuFe_2O_4$−NiO Nanocomposites

sample	υ_1 [cm^{-1}]	intensity I_{υ_1}	υ_2 [cm^{-1}]	intensity I_{υ_2}	band gap from UV–vis spectra [eV]
$CuFe_2O_4$	577.44	11.42	403.84	33.27	2.63
$CuFe_2O_4$−1% NiO	581.48	19.98	408.57	20.66	2.54
$CuFe_2O_4$−5% NiO	582.39	13.86	405.60	13.80	2.72
$CuFe_2O_4$−10% NiO	581.07	10.08	404.86	12.44	2.40
$CuFe_2O_4$−20% NiO	587.98	11.42	403.47	10.98	2.67

The experimentally determined and the theoretically calculated EXAFS functions in *k*-space and their Fourier transforms in real space for 5% and 20 wt % NiO containing $CuFe_2O_4$ nanocomposites, measured at the Fe K-edge, are shown in Figure 3, and the obtained structural parameters are listed in Table 2.

The structural parameters determined from the Fe K-edge measurements for 5% and $CuFe_2O_4$−20% NiO nanocomposites are nearly similar to each other and resemble those of $CuFe_2O_4$ nanoparticles.[48] However, the comparison of the Fourier transform plots of the two nanocomposites shows significant differences in the shape of the second peak. In $CuFe_2O_4$−5% NiO nanocomposites, the second peak is broad whereas in the case of $CuFe_2O_4$−20% NiO nanocomposites a distinct shoulder-like feature could be noticed. These variations could be attributed to the possible upsets in the ferric balance due to the displacement of metal cations. Similar observations have also been reported for NiZn ferrites.[57]

The experimentally determined and the theoretically calculated EXAFS functions in *k*-space and their Fourier transforms in real space for 5% and 20 wt % NiO containing $CuFe_2O_4$ nanocomposites, measured at the Ni K-edge, are shown in Figure 4, and the determined structural parameters are tabulated in Table 2.

The EXAFS spectra of 5% and 20% $CuFe_2O_4$−NiO nanocomposites are similar to each other and in the analysis of the EXAFS function; a three-shell model could be fitted for both the nanocomposites. The first shell consisting of about six oxygen backscatterers was found at 2.03 Å distance, the second shell having about six metal backscatterers was determined at a distance of about 2.92 Å, and the third shell with about six metal backscatterers was fitted at about 3.43 Å distance. The EXAFS obtained parameters are in good agreement with the structural parameters of $NiFe_2O_4$.[58] The results indicate the formation of $NiFe_2O_4$ during the preparation of $CuFe_2O_4$−NiO nanocomposites. Furthermore, the determined interatomic distances of 2.03 and 2.92 Å are also in accord with the Ni−O and Ni−Ni distances in NiO.[59] This result is in accordance with the XRD studies, which indicated the presence of the Bragg peaks characteristic of NiO, $NiFe_2O_4$, and also CuO.

3.3. XANES Investigations. The XANES investigations were performed in order to complement the results obtained from EXAFS studies. The XANES spectra of 5% and 20% $CuFe_2O_4$−NiO nanocomposites measured at the Cu K-edge is shown along with spectra of $CuFe_2O_4$ and CuO in Figure 5.

The XANES region of 5% $CuFe_2O_4$−NiO nanocomposites coincides with that of $CuFe_2O_4$ nanoparticles. But, in the near-edge region of the 20% $CuFe_2O_4$−NiO nanocomposites the pre-edge feature (marked as A in Figure 6) characteristic of CuO could be evidenced. This feature corresponds to 1s → 4p transition combined with the simultaneous "shake-down" transition of a high-energy electron into the Cu 3d hole.[60] The XANES investigations further strengthen the results obtained from the EXAFS analysis. The XANES regions at the Fe and Ni K-edges show no remarkable features and hence are not shown. The edge energy and oxidation states determined from the XANES analysis for $CuFe_2O_4$−NiO nanocomposites and the reference compounds at the Cu, Fe, and Ni K-edges are tabulated in Table 3. The comparison of the absorption edge values of $CuFe_2O_4$−NiO nanocomposites with the corresponding reference compounds indicate that copper, iron, and nickel are in +2, +3, and +2 oxidation states, respectively, in the nanocomposites.

3.4. FT-IR and UV–vis Investigations. FT-IR spectroscopy is an important tool to identify the stretching and bending vibrations of tetrahedral and octahedral complexes of ferrite materials. Figure 6 shows the FT-IR spectra of $CuFe_2O_4$−*x*NiO (x = 0, 1, 5, 10, and 20 wt %) nanocomposites measured in the frequency range of 400–1200 cm^{-1}, and the observed band values are given in Table 4. In general, the band around 600 cm^{-1} (υ_1) corresponds to intrinsic stretching vibration of metal cations at the tetrahedral site, while the band around 400 cm^{-1} (υ_2) corresponds to metal cations in the octahedral sites.[61] From Table 4 the observed values in the present case confirms the stretching and bending vibration of Fe^{3+}−O^{2-} complexes occupied in both the sites. Similarly, the intensity of the band values of υ_1 decreases with increasing the concentration of NiO compared with parent $CuFe_2O_4$, which implies the formation of $NiFe_2O_4$ and also the phase transition behavior from tetragonal to cubic.[62] The intensity of band values of υ_2 decreases with increasing concentration of NiO, which is due to the migration of Fe^{3+} ions from B-site to A-site.

The UV–vis spectra of 1100 °C sintered $CuFe_2O_4$−*x*NiO (x = 0, 1, 5, 10, and 20 wt %) nanocomposites is shown in Figure 7. The optical band gap (E_g) values are calculated using the plots of $(\alpha E)^2$ vs photon energy (plots not shown).[63] The calculated band gap values are given in Table 4. The band gap values suggest that the synthesized materials are

(58) Subramanyam, K. N. *J. Phys. C* **1971**, *4*, 2266.
(59) Cairns, R. W.; Ott, E. *J. Am. Chem. Soc.* **1933**, *55*, 527.
(60) Tranquada, J. M.; Heald, S. M.; Moodenbaugh, A. R. *Phys. Rev. B* **1987**, *36*, 5263.
(61) Berchmans, L. J.; Selvan, R. K.; Kumar, P. N. S.; Augustin, C. O. *J. Magn. Magn. Mater.* **2004**, *279*, 173.
(62) Kasapoglu, N.; Birsoz, B.; Baykal, A.; Koseoglu, Y.; Toprak, M. S. *Cent. Eur. J. Chem.* (DOI: 10.2478/s11532-007-0005-0).
(63) Zhang, D.; Fu, H.; Shi, L.; Pan, C.; Li, Q.; Chu, Y.; Yu, W. *Inorg. Chem.* **2007**, *46*, 2446.

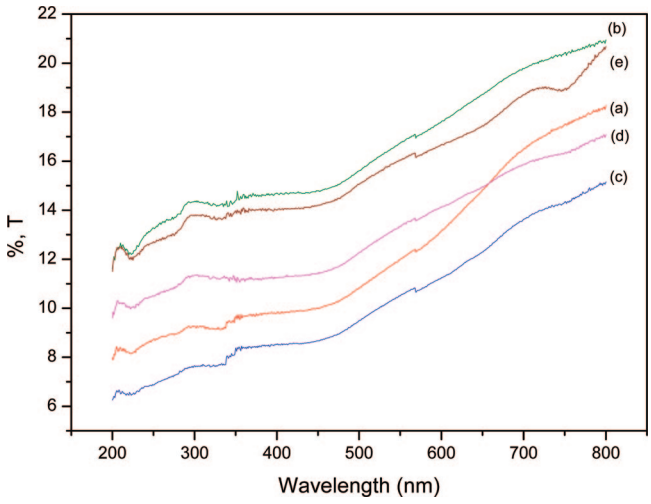

Figure 7. UV–vis spectra of $CuFe_2O_4$−x% NiO nanocomposites: (a) x = 0, (b) x = 1, (c) x = 5, (d) x = 10, and (e) x = 20.

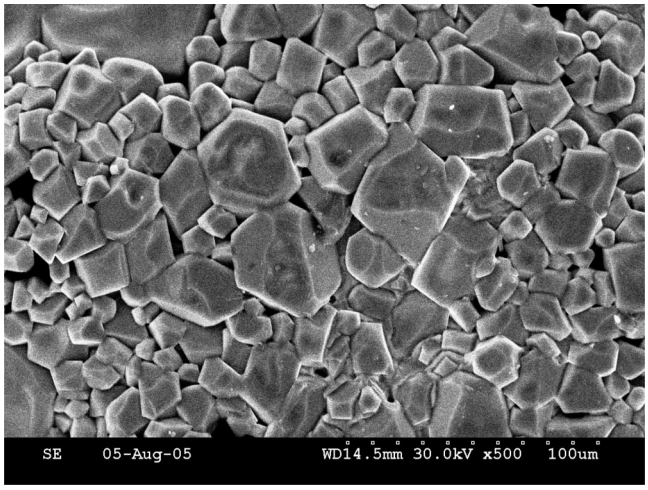

Figure 8. SEM image of $CuFe_2O_4$−5% NiO nanocomposites sintered at 1100 °C.

semiconductors. It can be observed that the nanocomposite samples do not exhibit any linear trend based on the concentration of NiO. The maximum band gap value of 2.72 eV is observed for $CuFe_2O_4$−5% NiO nanocomposite, which is higher than the parent $CuFe_2O_4$. This could be due to the quantum confinement effect when the size of the particle is reduced to nanoscale.[64]

3.5. Morphological Properties. The representative SEM image of 1100 °C-sintered $CuFe_2O_4$−5% NiO is shown in Figure 8. The image shows the particles are well-defined with definite grain boundaries. The grain-to-grain connectivity is reflected, and some air holes are also observed that may be due to the evaporation of volatile compounds at high temperature sintering. Interestingly, no particle agglomeration could be observed.

The representative TEM, HRTEM, and SAED images of nanocrystalline $CuFe_2O_4$−5% NiO nanocomposites are shown in Figure 9. The TEM image of the as-prepared $CuFe_2O_4$−5% NiO shows that the particles are more or less uniformly distributed with the particle size in the range of 5–10 nm. The HRTEM image shows the well-defined interlayer spacing of the particles and enumerates the crystallinity of the as-synthesized materials. The SAED pattern confirms the polycrystalline behavior of the materials.

3.6. Electrical Properties. In general, the electrical property of the ferrite materials depends on the method of preparation, chemical composition, grain size, and sintering temperature. Figure 10 illustrates the frequency dependence of the dielectric constant of $CuFe_2O_4$−xNiO (x = 0, 1, 5, 10, and 20 wt %) nanocomposites measured at room temperature. It can be seen that all the samples show the frequency-dependent phenomena indicating the decrease in dielectric constant value with increasing frequency. This is a normal behavior observed in most of the ferrimagnetic materials, which could be attributed to interfacial polarization as described by Maxwell and Wagner.[65] The polarization results in an electronic exchange between the ferrous and ferric ions, which produce local displacements in the direction of applied external field. Similarly, the $Ni^{3+} \leftrightarrow Ni^{2+} + e^+$ (e^+ denotes a hole) gives the hole concentration in the octahedral sites which produce the local displacements in the opposite direction of the applied fields. These displacements determine the polarization as well as the dielectric properties. At higher frequency, the dielectric constant values remain constant with increase in frequency due to the fact that, above certain frequencies, the electronic exchange between the ferrous and ferric ions does not follow the applied field. The compositional dependence of NiO on dielectric constant is also shown in Figure 10. Among all the compounds the lower dielectric constant value is observed at all measured frequencies for the $CuFe_2O_4$−20% NiO nanocomposites because the sample contains mainly $NiFe_2O_4$ and CuO components. Since $NiFe_2O_4$ shows a p-type conduction due to the hole exchange between Ni^{3+} and Ni^{2+}, so the value of dielectric constants are low.[66]

The variation of dielectric loss tangent with frequency for the samples of $CuFe_2O_4$−NiO nanocomposites is shown in Figure 11. It can be seen that an abnormal dielectric behavior could be observed for all the samples because the dielectric relaxation peaks result at a frequency of 20 kHz. A similar behavior has been reported in the Li−Mg ferrite system.[67] According to Rezlescu model,[68] these relaxation peaks may be due to the collective contribution of both p- and n-type of charge carriers. The electronic exchange between $Fe^{2+} \leftrightarrow Fe^{3+} + e^-$ and hole transfer between $Ni^{3+} \leftrightarrow Ni^{2+} + e^+$ in octahedral sites are responsible for such behaviors. Furthermore, the hopping frequencies of localized charge carriers are almost equal to that of the applied ac electric field.

The frequency dependence of ac electrical conductivity of all the samples is shown in Figure 12. It is observed that the ac conductivity increases with increasing applied frequency. Since the applied frequency enhances the hopping frequency of the charge carriers Fe^{2+} and Fe^{3+}, the conduction is increased. The conduction mechanism of ferrite is explained on the basis of

(64) Chang, S. M.; Doong, R. A. *J. Phys. Chem. B* **2004**, *108*, 18098.
(65) (a) Wagner, K. W. *Ann. Phys.* **1913**, *40*, 817. (b) Maxwell, J. C. *Electricity and Magnetism*; Oxford University Press: London, 1973; p 328.
(66) Ahmed, M. A.; Ateia, E.; El-Gamal, A. A. *Mater. Chem. Phys.* **2005**, *92*, 310.
(67) Bellad, S. S.; Watewe, S. C.; Chouglue, B. K. *Mater. Res. Bull.* **1999**, *34*, 1099.
(68) Rezlescu, N.; Rezlescu, E. *Phys. Status Solidi A* **1974**, *23*, 575.

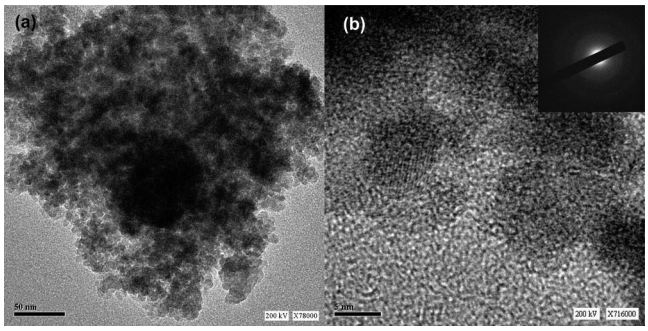

Figure 9. TEM (a), HRTEM (b), and SAED (inset) image of as-prepared $CuFe_2O_4$−5% NiO nanocomposites.

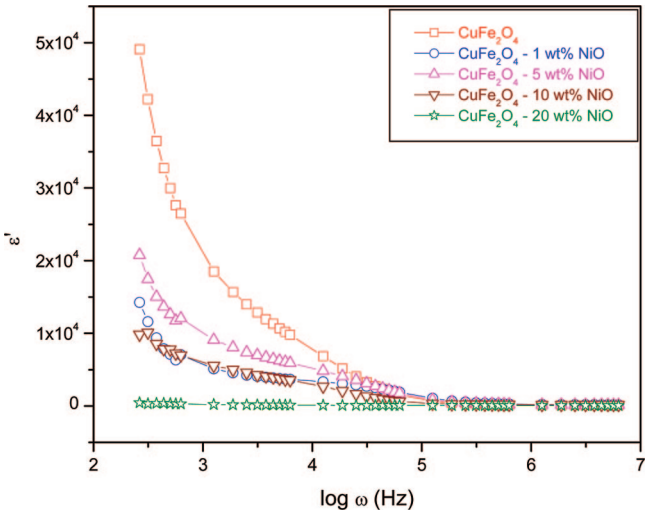

Figure 10. Dielectric constant (ϵ') vs frequency of $CuFe_2O_4$−NiO nanocomposites.

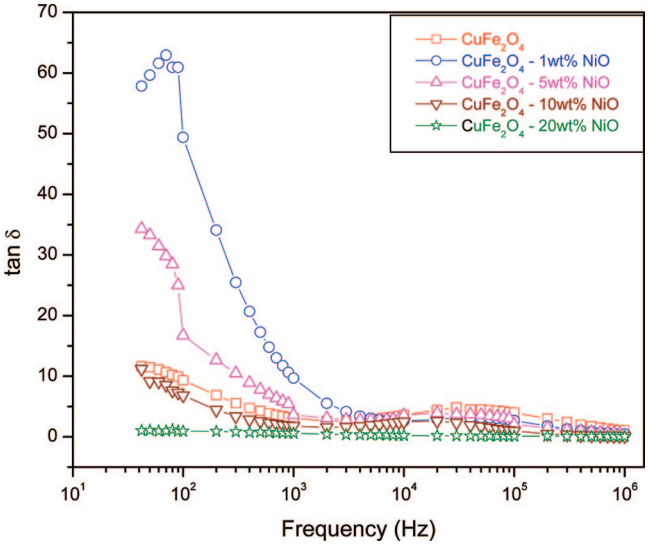

Figure 11. Dielectric loss tangent (tan δ) vs frequency of $CuFe_2O_4$−NiO nanocomposites.

hopping of charge carriers between the Fe^{2+} and Fe^{3+} on the octahedral sites. The compositional dependence on ac conductivity is also depicted in Figure 12. It can be seen that the magnitude of conductivity increases with increasing concentration of NiO on $CuFe_2O_4$ spinel. The maximum conductivity was obtained for $CuFe_2O_4$−20% NiO nanocomposite at 1 MHz, which could be attributed to the increased active carrier

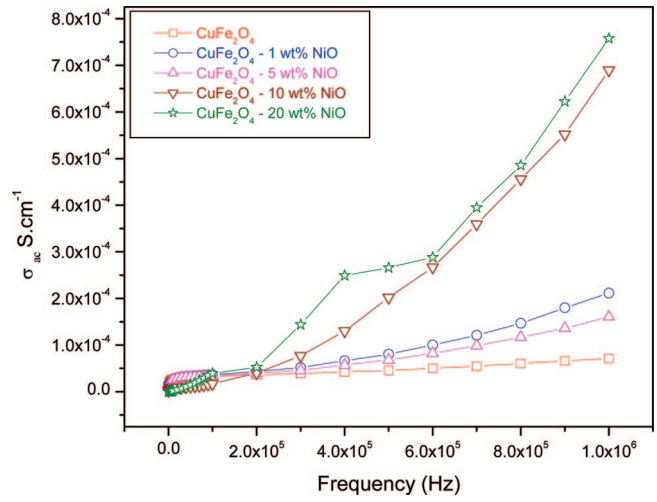

Figure 12. Ac conductivity vs frequency of $CuFe_2O_4$−NiO nanocomposites.

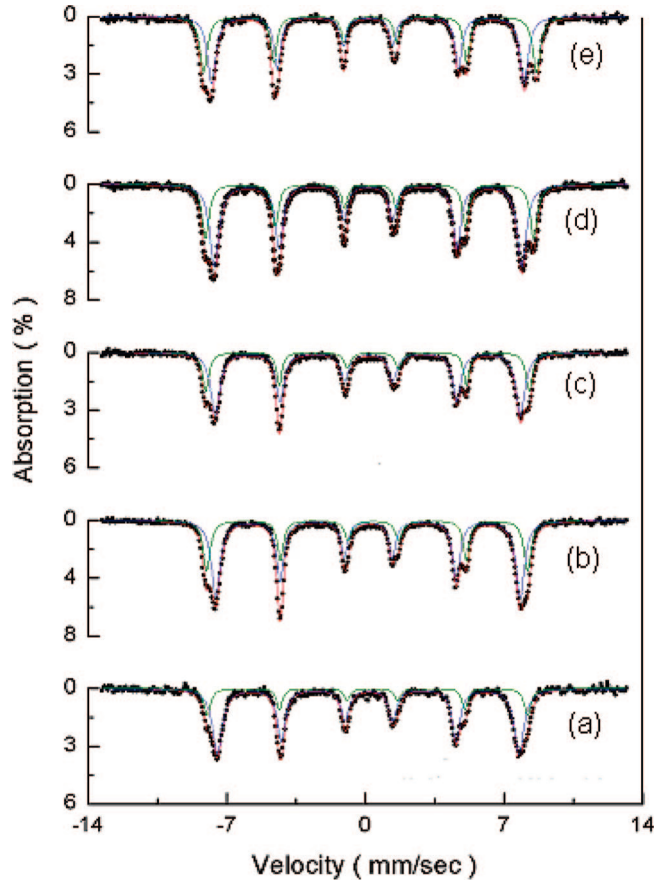

Figure 13. Mössbauer spectra of $CuFe_2O_4$−x% NiO nanocomposites: (a) $x = 0$, (b) $x = 1$, (c) $x = 5$, (d) $x = 10$, and (e) $x = 20$.

concentration with increasing concentration of NiO. Overall, the electrical properties of $CuFe_2O_4$−NiO nanocomposites are anomalous and do not follow any specific trend with regard to concentration of NiO. This could be ascribed to the presence of different phases, namely $CuFe_2O_4$, $NiFe_2O_4$, CuO, NiO, and Fe_2O_3, due to the exchange reactions (according to thermodynamics) and the phase segregation. In addition, the electrical properties mainly depend on the majority ferrite phase, particle size, density, and amount of secondary phases. A similar type

Table 5. Mössbauer Parameters for $CuFe_2O_4$−NiO Nanocomposites

sample	HF(B)[a] [kOe]	HF(A)[a] [kOe]	EQ(B)[b] [mm s^{-1}]	EQ(A)[b] [mm s^{-1}]	IS(B)[c] [mm s^{-1}]	IS(A)[c] [mm s^{-1}]
$CuFe_2O_4$	501.87	473.52	−0.12	−0.01	0.24	0.16
$CuFe_2O_4$−1% NiO	503.44	477.43	−0.16	−0.01	0.25	0.15
$CuFe_2O_4$−5% NiO	507.34	478.80	−0.14	−0.02	0.25	0.15
$CuFe_2O_4$−10% NiO	515.13	482.39	−0.02	0.00	0.25	0.15
$CuFe_2O_4$−20% NiO	522.51	490.34	−0.00	0.00	0.25	0.14

[a] HF = hyperfine field. [b] EQ = electric quadrupole splitting. [c] IS = isomer shift.

of observation has been reported for $Li_{0.35}Cd_{0.3}Fe_{2.35}O_4$−$SiO_2$ nanocomposite.[69]

3.7. Magnetic Properties. The room temperature Mössbauer spectra of 1100 °C-sintered $CuFe_2O_4$−xNiO (x = 0, 1, 5, 10, and 20 wt %) nanocomposites are shown in Figure 13. All the spectra were fitted with two subspectra: one for the tetrahedral (A) site and another for the octahedral (B) site due to the occupation of Fe^{3+} ions in both the sites. The results indicate that all the synthesized materials have inverse spinel structure. The calculated Mössbauer parameters such as magnetic hyperfine field values, isomer shift, and quadrupole splitting are given in Table 5. It can be seen that the magnetic hyperfine field value of B-sites is larger than the A-sites, which increases with increasing concentration of NiO on both sites. It is attributed to the super transferred hyperfine field mechanism of spinel compounds.[70] According to the literature,[48] in $CuFe_2O_4$ the Cu^{2+} ions occupy B-sites and Fe^{3+} ions occupy both -A and B-sites. When the concentration of NiO increases in the host structure, some of the Fe^{3+} ions are migrated from B-site to A-site due to the preferential occupancy of Ni^{2+} for B-sites. So the replacement of nonmagnetic ion by a magnetic ion will produce an increase of the super transferred hyperfine contribution at both the sites. This leads to the increase in hyperfine field values of both A- and B-sites in all the samples.[71] This may also be due to the higher magnetic moment of Ni^{2+} (2 μ_B^{-1}) than the Cu^{2+} (1 μ_B^{-1}).

The isomer shift values are slightly changed with NiO addition, which shows that the s-electron charge distributions of Fe^{3+} ions are negligibly influenced by the NiO addition.[72] In all the composites the isomer shift values indicate that the Fe ions are in +3 oxidation state. The isomer shift and hyperfine values are slightly enhanced in B-sites compared with A-sites, which may be due to the higher degree of covalent bonding in the tetrahedral cation sublattice. The quadrupole splitting values of the nanocomposites reveal tetragonal structure for $CuFe_2O_4$ for 1% and 5% NiO-containing samples, whereas cubic structure could be observed for 10% and 20% NiO-containing samples. In addition, the observed electric quadrupole splitting (EQ) values are ∼0.00 mm s^{-1}, in accordance with the XRD results.

4. Conclusions

$CuFe_2O_4$−xNiO (x = 1, 5, 10, and 20 wt %) nanocomposites have been prepared by the one-pot combustion method. The structural investigations of the prepared samples reveal the composite nature for $CuFe_2O_4$−NiO materials. EXAFS and XANES investigations substantiate the XRD results revealing the formation of $NiFe_2O_4$ and CuO, in addition to the existence of $CuFe_2O_4$ and NiO phases. The FT-IR studies reveal the characteristic stretching and bending vibrations of the octahedral and tetrahedral subunits of the nanocrystalline ferrites. The band gap of the materials has been determined using UV–vis spectroscopic studies, which also indicate the quantum size confinement effects. The TEM and HRTEM images confirm that the synthesized materials are nanocrystalline, thereby revealing their particle sizes. The SEM image clearly elucidates the grain-to-grain connectivity. The dielectric behavior investigations enumerate the normal ferrimagnetic nature of the materials, while the ac conductivity studies indicate an increase in specific conductivity with increase in NiO concentration attributable to the synergistic contribution of holes and electrons. The Mössbauer studies elucidate the inverse spinel structure of the prepared materials and also substantiate the phase transition behavior.

Acknowledgment. HASYLAB at DESY, Hamburg, is gratefully acknowledged for the kind support of the synchrotron radiation experiments at beamline A1. The authors express their gratitude to Prof. A. K. Shukla, Director, CECRI, Karaikudi, India, for his keen interest in this work.

CM701937Q

(69) Kotnala, R. K.; Verma, V.; Pandey, V.; Awana, V. P. S.; Aloysius, R. P.; Kothari, P. C. *Solid State Commun.* **2007**, *143*, 527.
(70) Singhal, S.; Chandra, K. *J. Solid State Chem.* **2007**, *180*, 296.
(71) Muthusamy, P.; Nagarajan, T.; Narayanasamy, A. *J. Phys. C* **1982**, *15*, 2519.
(72) Roumaih, K.; Manapov, R. A.; Sadykov, E. K. *J. Magn. Magn. Mater.* **2005**, 288.